Smart Mater. Struct. **7** (1998) 95–104. Printed in the UK PII: S0964-1726(98)88077-4

Vibration suppression of a spacecraft flexible appendage using smart material*

John L Meyer†, William B Harrington†, Brij N Agrawal and Gangbing Song

Department of Aeronautics and Astronautics, US Naval Postgraduate School, Monterey, CA 93943, USA

Received 21 July 1997, accepted for publication 15 September 1997

Abstract. This paper presents the results of positive position feedback (PPF) control and linear–quadratic Gaussian (LQG) control for vibration suppression of a flexible structure using piezoceramics. Experiments were conducted on the US Naval Postgraduate School's flexible spacecraft simulator (FSS), which is comprised of a rigid central body and a flexible appendage. The objective of this research is to suppress the vibration of the flexible appendage. Experiments show that both control methods have unique advantages for vibration suppression. PPF control is effective in providing high damping for a particular mode and is easy to implement. LQG control provides damping to all modes; however, it cannot provide high damping for a specific mode. LQG control is very effective in meeting specific requirements, such as minimization of tip motion of a flexible beam, but at a higher implementation cost.

1. Introduction

The current trend of spacecraft design is to use large, complex and light-weight space structures to achieve increased functionality at a reduced launch cost. The combination of large and light-weight design results in these space structures being extremely flexible and having low-frequency fundamental vibration modes. These modes might be excited in a variety of tasks such as slewing, pointing maneuvers and docking with other spacecraft. To effectively suppress the induced vibration poses a challenging task for spacecraft designers. One promising method for this problem is to use embedded piezoelectric materials as actuators (compensators) since piezoelectric materials have advantages such as high stiffness, light weight, low power consumption and easy implementation.

A wide range of approaches have been proposed for using piezoelectric material to actively control vibration of flexible structures. Positive position feedback (PPF) (Goh and Caughey 1985, Fanson and Caughey 1990, Agrawal and Bang 1994) was applied by feeding the structural position coordinate directly to the compensator and the product of the compensator and a scalar gain positively back to the structure. PPF offers quick damping for a particular mode provided that the modal characteristics are well known. PPF is also easy to implement. Linear–quadratic Gaussian (LQG) design was also applied (Won *et al* 1994, Agrawal 1996). The control input of LQG is designed to optimize the weighted sum of the quadratic indices of energy (control input) and performance. By adjusting the weights, LQG design can meet a specific requirement, for example, to minimize the tip deflection and rotation of a flexible structure. Strain rate feedback (SRF) control was used for active damping of a flexible space structure (Newman 1992). In this approach, the structural velocity coordinate is fed back to the compensator and the compensator position coordinate multiplied by a negative gain is fed back to the structure. SRF has a wider active damping region and can stabilize more than one mode given a sufficient bandwidth. Fuzzy control was utilized to control the vibration of a flexible robot manipulator (Zeinoun and Khorrami 1994). This method demonstrated robust performance in the presence of large payload variation. H_∞ control was applied to flexible structures which have uncertainty in the modal frequencies and damping ratios (Smith *et al* 1994). Other methods include model reference control (MRC) (Gopinathan and Pajunen 1995) and phase lead control (Feuerstein 1996).

In this paper we present the application of PPF control and LQG control to vibration suppression of a flexible structure by using embedded piezoceramic actuators. The flexible structure to be controlled is a two-link armlike flexible appendage on the flexible space simulator (FSS) at the US Naval Postgraduate School. Since modal characteristics of the flexible appendage

† Now with Naval Research Laboratory, Washington, DC 20375, USA.

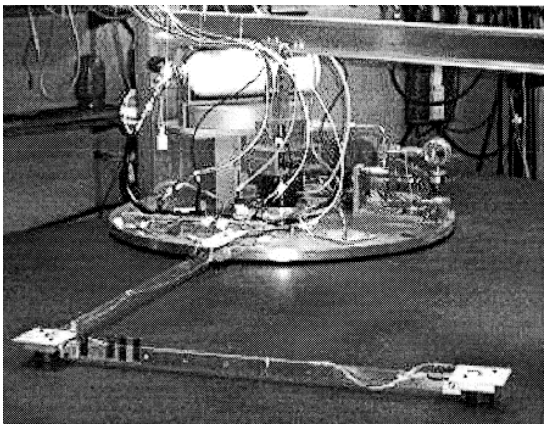

Figure 1. Flexible spacecraft simulator (FSS).

can be obtained prior to the control design via FEM analysis and experimental testing, PPF is used to achieve fast damping of the vibration of a particular mode. Application of PPF to multi-mode vibration suppression was also studied. The PPF controller was implemented on the flexible appendage in a cantilevered configuration utilizing piezoelectric sensor output representing structural displacement. Control of induced vibrations was performed by applying control signals to piezoelectric actuators. Both numerical simulations and experimental results demonstrate that PPF significantly increases damping for single-mode vibration suppression and in the multiple-mode case damping is moderately increased. Linear–quadratic Gaussian (LQG) control is used to minimize the tip displacement and rotation with the help of additional hardware (LEDs and CCD camera) which detects the tip displacement and rotation. Experiments show that the LQG method provides high active damping in both single-mode and multi-mode excitations but at a higher implementation cost.

2. Experimental setup

The flexible spacecraft simulator (FSS) simulates motion about the pitch axis of a spacecraft. As shown in figure 1 it is comprised of a rigid central body and a reflector supported by a two-link armlike flexible appendage. The center body represents the main body of the spacecraft while the flexible appendage represents a flexible antenna support structure. The flexible appendage is composed of a base beam cantilevered to the main body and a tip beam connected to the base beam at a right angle with a rigid elbow joint. In this experiment, the main body is fixed relative to the granite table. The flexible appendage is supported by one air pad each at the elbow and tip to minimize the friction effect.

Measurement of the motion of the flexible appendage is accomplished by a full complement of sensors. Figure 2 shows piezoceramic patches mounted at the root of the base beam and tip beam to measure strain in the flexible appendage. An optical infrared sensing camera shown in figure 3 provides position and rate information for designated LED targets mounted on the structure. Groups of targets are mounted on the main body in addition to the elbow joint and tip of the flexible appendage. This camera is mounted 1.9 meters above the granite table assembly. The camera is connected to a 68030 microprocessor running a real-time operating system, *VxWorks*. The 12-bit digital data obtained by the camera are ported out of the 68030 via a digital-to-analog converter card at 60 Hz sampling frequency. The camera's resolution is nominally at the sub-pixel level of the order of 1/20th of a pixel which leads to a camera accuracy of approximately 0.5 mm.

Data acquisition and control of the FSS is accomplished with a rapid design prototyping and real-time control system—an Integrated Systems AC-100. The AC-100 consists of a VAXstation 3100 host machine and an Intel 80386 real-time control processor. The host machine and control processor are connected via ethernet. Real-time code is developed on the host machine using MATRIX_X and SystemBuild and is downloaded to the control processor for implementation. Analog sensor data from the system are directly accessed by the control processor through on-board analog-to-digital (A/D) converters. All sensor connections are single ended due to restrictions on hardware functionality. Consequently, this condition will introduce noise in all sensor measurements. Likewise, the generated digital control data are converted to analog signals and output to the structure actuators. All A/D and D/A inputs are bipolar with a voltage range of ± 10 volts. A high-voltage amplifier is used on the piezoceramic actuator signals to increase the control authority by a factor of 15. This gain on the signal significantly enhances the structural control capabilities without running the risk of de-poling the piezoceramic actuators.

3. System modeling

The flexible appendage is modeled using the finite-element method. It was determined that no more than the three lowest modes are significant in the response of the appendage and thus would be considered in the simulations. For the analysis, six elements were used to characterize the structure. Elements 1 and 4 are piezoceramic actuator elements, elements 2 and 5 are piezoceramic sensor elements and elements 3 and 6 are simple aluminum beam elements. Point masses were added to the elbow joint and tip to represent the connection brackets and air pads. Figure 4 shows the element configuration and measurements. The basic elements were formulated using the direct method of derivation but were subsequently augmented with the mass and stiffness properties of the piezoelectric patches. Table 1 gives the material properties used in modeling the appendage and table 2 gives piezoceramic properties.

The beam element for the finite-element model is shown in figure 5. In addition, electro-mechanical relationships of the piezoelectric material must be considered for implementation in an analytical model suitable for control design and simulation.

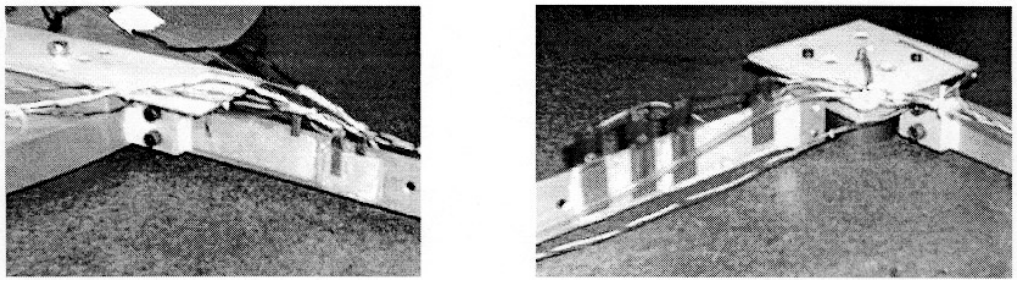

Figure 2. Base joint (left) and elbow joint (right) with piezoceramic actuator and sensor patches and LED targets.

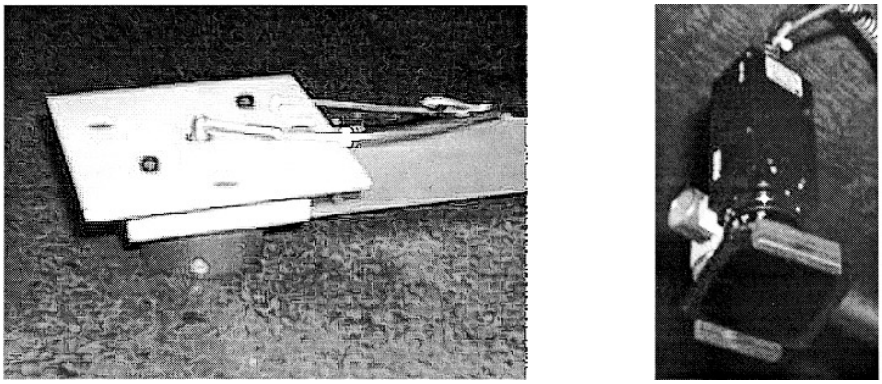

Figure 3. Flexible appendage tip with LED targets (left) and optical infrared sensing camera (right).

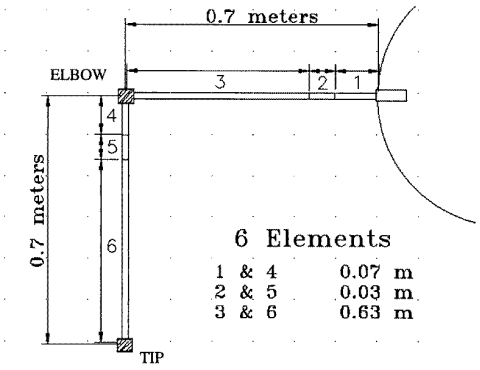

Figure 4. FEM configuration of the flexible appendage.

Table 1. Material properties of flexible appendage.

Property	Symbol	Units	Value
Beam thickness	t_b	meters	1.5875×10^{-3}
Beam width	w_b	meters	2.54×10^{-2}
Beam density	ρ_b	kg m^{-3}	2.800×10^{3}
Young's modulus	E_b	N m^{-2}	1.029×10^{7}

The general relationship for the electro-mechanical coupling is given by

$$\begin{Bmatrix} D_3 \\ S_1 \end{Bmatrix} = \begin{bmatrix} \varepsilon_3^T & d_{31} \\ d_{31} & s_{11}^E \end{bmatrix} \begin{Bmatrix} E_3 \\ T_1 \end{Bmatrix} \tag{3.1}$$

where D is the displacement, S is the strain, E is the electric field, T is the stress, s is the compliance and d is the piezoelectric constant. The subscripts are tensor notation where the 1- and 2-axes are arbitrary in the plane perpendicular to the 3-axis poling direction of the piezoelectric material. Using the fact that the elastic constant for piezoceramic material, s, is the inverse of its Young's modulus, E_p, this equation can be written as

$$\begin{Bmatrix} D_3 \\ T_1 \end{Bmatrix} = \begin{bmatrix} \varepsilon_3^T - d_{31}^2 E_p & d_{31} E_p \\ -d_{31} E_p & E_p \end{bmatrix} \begin{Bmatrix} E_3 \\ S_1 \end{Bmatrix}. \tag{3.2}$$

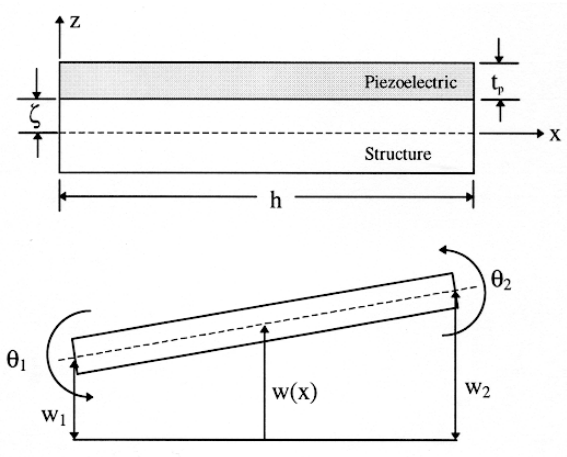

Figure 5. Beam element for finite-element model.

Table 2. Material properties of piezoceramics.

Property	Symbol	Units	Value
Lateral strain coefficient	d_{31}	m V^{-1} or C N^{-1}	1.8×10^{-10}
Young's modulus	E_p	N m^{-2}	6.3×10^{10}
Poisson's ratio	ν	N A^{-1}	0.35
Absolute permittivity	D	F m^{-1} or N V^{-2}	1.5×10^{-8}

The equation for the elemental potential energy is given by

$$-U = \tfrac{1}{2}\int \left(-T_1 S_1 + D_3 E_3\right) \mathrm{d}V \tag{3.3}$$

where the two terms in the integral represent mechanical energy and electrical energy respectively. Using w_p as the width of the piezoceramic wafer, this equation can be rewritten as

$$\begin{aligned} -U &= \frac{1}{2} w_p \int_0^h \int_\zeta^{\zeta+t_p} \left(-T_1 S_1 + D_3 E_3\right) \mathrm{d}x\, \mathrm{d}z \\ &= \frac{1}{2} w_p \int_0^h \int_\zeta^{\zeta+t_p} \begin{Bmatrix} D_3 \\ T_1 \end{Bmatrix}^T \begin{bmatrix} 1 & 0 \\ 0 & -1 \end{bmatrix} \begin{Bmatrix} E_3 \\ S_1 \end{Bmatrix} \\ &\quad \mathrm{d}x\, \mathrm{d}z. \end{aligned} \tag{3.4}$$

The strain, using small-angle displacement theory, S_1, can be written as

$$S_1 = \varepsilon_x = -z\left(\partial^2 w / \partial x^2\right) \tag{3.5}$$

where w is the bending displacement along the x-axis. Substituting (3.2) into (3.4), we have

$$\begin{aligned} -U &= \tfrac{1}{2} w_p \int_0^h \int_\zeta^{\zeta+t_p} \begin{Bmatrix} E_3 \\ \varepsilon_x \end{Bmatrix}^T \begin{bmatrix} \varepsilon_e^T - d_{31}^2 E_p & d_{31} E_p \\ d_{31} E_p & -E_p \end{bmatrix} \\ &\quad \times \begin{Bmatrix} E_3 \\ \varepsilon_x \end{Bmatrix} \mathrm{d}x\, \mathrm{d}z \\ &= \tfrac{1}{2} w_p \int_0^h \int_\zeta^{\zeta+t_p} \left[\left(\varepsilon_3^T - d_{31}^2 E_p\right) E_3^2 + 2 d_{31} E_p E_3 \varepsilon_x \right. \\ &\quad \left. - E_p \varepsilon_x^2\right] \mathrm{d}x\, \mathrm{d}z \end{aligned} \tag{3.6}$$

then using equation (3.5) results in

$$\begin{aligned} -U = \tfrac{1}{2} w_p \int_0^h \int_\zeta^{\zeta+t_p} &\left\{\left(\varepsilon_3^T - d_{31}^2 E_p\right) E_3^2 \right. \\ &\left. + 2 d_{31} E_p E_3 z \frac{\partial^2 w}{\partial x^2} - E_p z^2 \left(\frac{\partial^2 w}{\partial x^2}\right)^2\right] \mathrm{d}x\, \mathrm{d}z. \end{aligned} \tag{3.7}$$

The bending displacement can be written in terms of its modal decomposition as

$$w(x,\, t) = \sum_{i=1}^{4} \Phi_i(x) q_i(t) \tag{3.8}$$

where $\Phi \in \mathcal{R}^4$ is the vector of interpolation functions or 'mode shapes' and $q \in \mathcal{R}^4$ is the nodal displacement vector or state vector. Substituting (3.8) into (3.7) gives the general form of the energy equation

$$-U = \tfrac{1}{2}\gamma e^2 - q^T b e - \tfrac{1}{2} q^T k_p q \tag{3.9}$$

where

$$\gamma = w_p h\left(\varepsilon_3^T - d_{31}^2 E_p\right) \Big/ t_p \qquad e = t_p E_3$$

$$b_i = d_{31} E_p w_p \left(\zeta + \tfrac{1}{2} t_p\right) \int_0^h \frac{\mathrm{d}^2 \Phi_i(x)}{\mathrm{d}x^2}\, \mathrm{d}x$$

$$\left[k_p\right]_{ij} = w_p E_p t_p \left[\zeta^2 + \zeta t_p + \tfrac{1}{3} t_p^2\right] \int \frac{\mathrm{d}^2 \Phi_i(x)}{\mathrm{d}x^2} \frac{\mathrm{d}^2 \Phi_j(x)}{\mathrm{d}x^2}\, \mathrm{d}x$$

(for $i = 1, \ldots, 4$; $j = 1, \ldots, 4$).

Substituting the interpolation functions Φ into the b vector gives

$$\begin{aligned} b_1 &= 0 \qquad & b_2 &= -d_{31} E_p w_p \left(\zeta + t_p/2\right) \\ b_3 &= 0 \qquad & b_4 &= d_{31} E_p w_p \left(\zeta + t_p/2\right). \end{aligned} \tag{3.10}$$

The piezoceramic elemental stiffness matrix is identical to the general elemental stiffness matrix with the exception that the piezoelectric stiffness κ replaces the structural stiffness. κ is given by

$$\kappa = w_p t_p E_p \left(\zeta^2 + \zeta t_p + t_p^2/3\right). \tag{3.11}$$

By including the effect of elastic energy of the beam element, we can write (3.9) as

$$-U = \tfrac{1}{2}\gamma e^2 - q^T b e - \tfrac{1}{2} q^T k q \tag{3.12}$$

where $k = k_b + k_p$, k_b is the stiffness matrix for the structure and k_p is the stiffness matrix for the piezoelectric material.

The kinetic energy for the piezoelectric material can be written as

$$T = \tfrac{1}{2} \dot{q}^T M \dot{q} \tag{3.13}$$

where $M = M_b + M_p$, M_b is the mass matrix for the structure and M_p is the mass matrix for the piezoelectric material.

The Lagrangian function, L, is given by

$$L = T - U = \tfrac{1}{2} \dot{q}^T M \dot{q} + \tfrac{1}{2}\gamma e^2 - q^T b e - \tfrac{1}{2} q^T k q. \tag{3.14}$$

Evaluation of the Lagrangian equation yields

$$[M]\ddot{q} + [K] q = -B e. \tag{3.15}$$

(3.15) represents the equation for the actuation. Taking e as the generalized coordinate, the equation in terms of e is given as

$$\gamma e = B^T q. \tag{3.16}$$

For structural elements that have piezoelectric material bonded to them, their respective mass and stiffness matrices are the sum of the beam elemental matrices and the piezoceramic elemental matrices.

Table 3. Natural frequencies of flexible arm model.

Mode	Frequency (Hz)
1	0.29583
2	0.87067
3	11.108
4	28.496
5	45.144
6	102.78

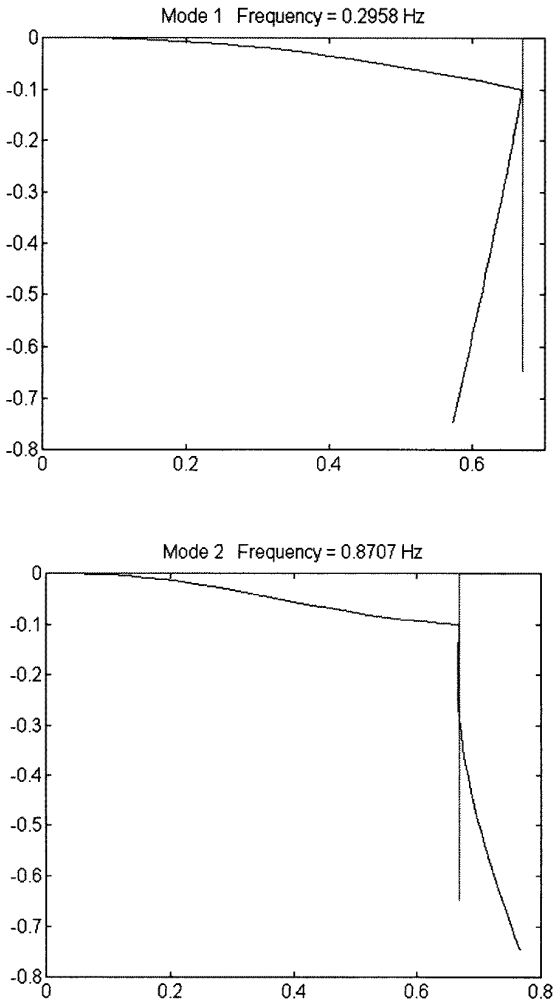

Figure 6. Modal shapes of first (top) and second (bottom) mode of flexible appendage.

Solution of the eigenvalue problem using the complete finite-element model yielded 12 modes and mode shapes. Table 3 gives the first six frequencies of oscillation and figure 6 shows the first two mode shapes. These two modes are the primary carriers of energy for the structure and will be actively controlled.

In the absence of the external input, the system dynamics are governed by

$$[M]\ddot{q} + [K]q = 0.$$

The desired equations of motion are of the form

$$[M]\ddot{q} + [C]\dot{q} + [K]q = 0 \tag{3.17}$$

where $[C]$ is the damping matrix for the system in physical coordinates.

Utilizing the linear similarity transformation

$$\dot{q} = S\Psi \qquad T = S^{-1} \qquad S = Tq \tag{3.18}$$

where S is chosen so that

$$S^T[M]S = I$$
$$S^T[C]S = \text{diag}(\ldots,\ 2\zeta\omega_i,\ \ldots) = [\Omega]$$
$$S^T[K]S = \text{diag}(\ldots,\ \omega_i^2,\ \ldots) = [\Lambda]$$

(3.17) can be transformed into a diagonal form in terms of the modal coordinate vector, Ψ

$$\ddot{\Psi} + [\Omega]\dot{\Psi} + [\Lambda]\Psi = 0 \tag{3.19}$$

which can be rewritten in state space form

$$\begin{Bmatrix} \dot{\Psi} \\ \ddot{\Psi} \end{Bmatrix} = A_m \begin{Bmatrix} \Psi \\ \dot{\Psi} \end{Bmatrix} \tag{3.20}$$

where

$$A_m = \begin{bmatrix} 0 & I \\ -[\Lambda] & -[\Omega] \end{bmatrix}.$$

The system (3.20) can be transformed back to the physical coordinates by utilizing $S = Tq$,

$$\begin{Bmatrix} \dot{q} \\ \ddot{q} \end{Bmatrix} = A \begin{Bmatrix} q \\ \dot{q} \end{Bmatrix} \tag{3.21}$$

where

$$A = \begin{bmatrix} T & 0 \\ 0 & T \end{bmatrix}^{-1} A_m \begin{bmatrix} T & 0 \\ 0 & T \end{bmatrix}.$$

Considering the external inputs, state noise and sensor noise, we can rewrite (3.21) as

$$\dot{x} = Ax + Bu + Fw \tag{3.22a}$$
$$y = Cx + v \tag{3.22b}$$

where $x = \{q^T,\ \dot{q}^T\}^T \in \mathcal{R}^{24}$ represents the translational and rotational displacements and velocities at node points of the finite-element model. $u \in \mathcal{R}^2$ denotes the control voltages of the base and elbow actuators. $y \in \mathcal{R}^6$ is the sensor output vector which consists of two piezoceramic sensor output voltages and four CCD camera outputs, representing elbow and tip displacements and rotations. $B \in \mathcal{R}^{24\times 2}$ is the input matrix. $C \in \mathcal{R}^{6\times 24}$ is the output matrix. $v \in \mathcal{R}^6$ represents the measurement noise. F is the plant uncertainty matrix and w is the state noise vector. The states are estimated using a Kalman filter.

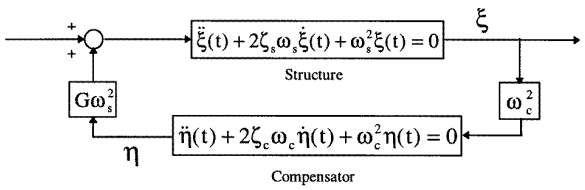

Figure 7. Positive position feedback block diagram.

4. Control design

4.1. Positive position feedback control

For control of the flexible appendage, the positive position feedback (PPF) control scheme shown in figure 7 is well suited to implementation utilizing the piezoelectric sensors and actuators. In PPF control methods, structural position information is fed to a compensator. The output of the compensator, magnified by a gain, is fed directly back to the structure. The equations describing PPF operation are given as

$$\begin{aligned} \ddot{\xi}(t) + 2\zeta_s\omega_s\dot{\xi}(t) + \omega_s^2\xi(t) &= G\omega_s^2\eta \\ \ddot{\eta}(t) + 2\zeta_c\omega_c\dot{\eta}(t) + \omega_c^2\eta(t) &= \omega_c^2\xi \end{aligned} \tag{4.1}$$

where ξ is a coordinate describing displacement of the structure, ζ_s is the damping ratio of the structure, ω_s is the natural frequency of the structure, G is the feedback gain, η is the compensator coordinate, ζ_c is the compensator damping ratio and ω_c is the frequency of the compensator.

The stability condition for the combined system in (4.1) is given as

$$\frac{\zeta_s\omega_s^3 + \zeta_c\omega_c^3 + 4\zeta_s\omega_s\zeta_c^2\omega_c^2}{(\zeta_s\omega_s + \zeta_c\omega_c)^2\omega_s\omega_c} < g < 1.$$

For more interpretation of the PPF compensator, we introduce a frequency domain analysis. Assume ξ is given as

$$\xi(t) = X\mathrm{e}^{\mathrm{i}\omega_s t}$$

then the output of the compensator is

$$\eta(t) = \frac{X\omega_s/\omega_c\,\mathrm{e}^{\mathrm{i}(\omega_s t - \phi)}}{\sqrt{(1-\omega_s^2/\omega_c^2)^2 + (2\zeta_c\omega_s/\omega_c)^2}}$$

where the phase angle ϕ is

$$\phi = \tan^{-1}\left(\frac{2\zeta_c\omega_s/\omega_c}{1-\omega_s^2/\omega_c^2}\right).$$

Therefore

$$\frac{\eta}{\xi} = \frac{\mathrm{e}^{-\mathrm{i}\phi}}{\sqrt{(1-\omega_s^2/\omega_c^2)^2 + (2\zeta_c\omega_s/\omega_c)^2}}.$$

The system frequency response characteristics are shown in figure 8. As seen in the figure, when the PPF compensator's frequency is in the region of the structure's natural frequency, the structure experiences active damping. Additionally, when ω_c is lower than ω_s, active flexibility results and when ω_c is larger than ω_s, active stiffness results. Clearly, to maximize damping in the structure, the compensator's frequency must be closely matched to ω_s.

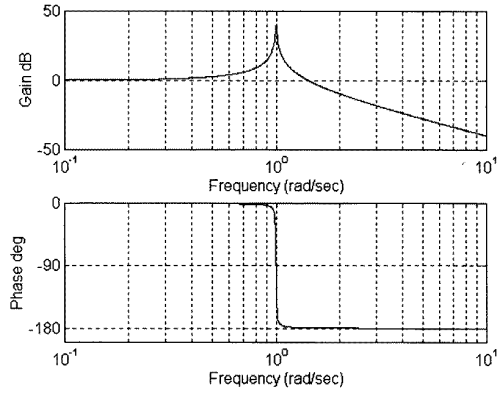

Figure 8. Frequency response of system to PPF controller. ω_s = 1 rad s^{-1}, ζ_s = 0.005, G = 1.

4.2. Linear–quadratic Gaussian control

To minimize the tip movement of the flexible appendage, the linear–quadratic Gaussian (LQG) method is used. The control voltages for the actuators are determined by the optimal control solution of the linear–quadratic regulator (LQR) problem of the system described by (3.22) with states estimated by a Kalman filter. The solution minimizes the performance index given by

$$J = \int \left(x^T Q x + u^T R u\right) \mathrm{d}t$$

where Q and R are weighting matrices for the states and control voltages respectively. The solution to the LQR problem seeks a compromise between minimum energy (control input) and best performance. Since the objective in this problem is to minimize the displacement and rotation at the tip of the flexible appendage, the weight values corresponding to these states are kept significantly high and the values of R are selected such that the control input voltage to the actuators is within their limitations of 150 volts. The control voltage is obtained as

$$u = -K_{LQR}x = -R^{-1}B^T G x$$

where G is the solution to the Riccati equation

$$-Q - A^T G - GA + GBR^{-1}B^T G = 0.$$

The Kalman filter is designed as

$$\dot{\hat{x}} = \left(A - BK_{LQR} - \hat{L}C\right)\hat{x} + \hat{L}y$$

where the optimum observed gain $\hat{L}$ is given by

$$\hat{L} = \hat{P}C'W^{-1}$$

where $\hat{P}$ is defined as

$$\dot{\hat{P}} = A\hat{P} + \hat{P}C^T - \hat{P}C^T W^{-1}C\hat{P} + FVF^T$$

where the process noise covariance matrices V and W are given by

$$\begin{aligned} E\left\{vv^T\right\} &= V(t)\delta(t-\tau) \\ E\left\{vw^T\right\} &= X(t)\delta(t-\tau) \\ E\left\{ww^T\right\} &= W(t)\delta(t-\tau) \end{aligned}$$

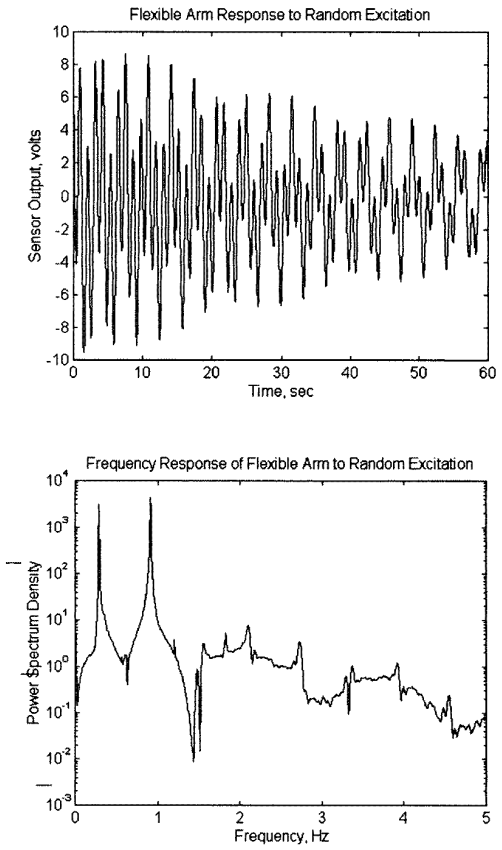

Figure 9. Response to random excitation and corresponding power spectrum density plot.

Table 4. Comparison of modal frequencies.

Mode	Experiment (Hz)	Model (Hz)	% error
1	0.2869	0.295 83	3.11
2	0.9169	0.870 67	5.04

and $X(t)$ is the system cross-covariance matrix, a function of the correlation of sensor noise to plant noise, and under most circumstances it is normally zero. The symbol $E\{\}$ denotes mathematical expectation.

5. Experimental results

5.1. Structural identification

Identification of the natural frequencies of the flexible appendage was performed by randomly exciting the structure and performing a discrete FFT. Figure 9 shows the response of the appendage to the excitation along with the corresponding power spectrum density. The first two modal frequencies were identified as 0.287 and 0.917 Hz respectively. Table 4 shows the comparison of experimentally obtained frequencies to those from the finite-element model.

The damping in first two modes was experimentally identified by employing the log decrement method given as

$$\zeta = \frac{1}{2\pi n} \ln\left(A_i/A_f\right) \tag{5.1}$$

where ζ is the damping, A_i is the initial amplitude, A_f is the final amplitude and n is the number of oscillations between.

Each mode was individually excited by imparting a sinusoidal input to the piezoelectric actuators at the frequency of the mode of interest. For each mode, the damping was identified as 0.3%.

5.2. PPF simulations and experiments

Figure 10–12 show the results of implementing a PPF controller on the flexible appendage using piezoelectric sensors as input and piezoelectric actuators as output. All these figures display data taken from the piezoelectric sensor located at the root of the base arm. Figure 10 shows the results of controlling a pure first-mode response. Figure 10(a) and (b) are simulations using Simulink and figure 10(c) and (d) are experimental results. For both cases, the structure's first mode was excited through sinusoidal input from the piezoelectric actuators at the first modal frequency. As seen in figure 10(a) and (c), due to the structure's light internal damping, the induced oscillation takes several minutes to damp out passively. Figure 10(b) and (d) show the actively controlled structure using a PPF controller. For this case, the frequency of the controller was set at the first modal frequency of the structure, the damping ratio was 1 and the feedback gain was 1. The feedback gain is set to maximize the control output within the ± 10 volt range of the A/D output of the digital controller. This helps maintain linear control signal output to the actuators. The log decrement method was again employed to evaluate the increased damping in the controlled structure. It was determined that the damping increased from 0.4% to 3% with PPF control, an increase of 650%.

Figure 11 shows the results of controlling a pure second-mode response. For this case, the frequency of the controller was set at the second modal frequency of the structure, the damping ratio was 1, and the feedback gain was 0.1. It was determined that the damping increase from 0.4% to 5.8% with PPF control, an increase of 1350%.

Figure 12 shows the results of controlling a combined first- and second-mode response. The excitation was produced by initially exciting the structure's first mode and then adding a second-mode excitation to the tip arm piezoelectric actuator. Figure 12(a) shows the free response of the structure to the excitation. Figure 12(b) shows the implementation of the PPF controller tuned to the first mode of vibration with a gain of 1. It shows good damping for the first mode but residual oscillations at the second-mode resonant frequency. Figure 12(c) shows the implementation of a PPF controller with the base arm actuator tuned to the first resonant frequency and the tip arm actuator tuned to the second resonant frequency. A gain of 1 was used for the base arm and 0.1 for the tip arm. The structure maintains good damping characteristics for the first mode

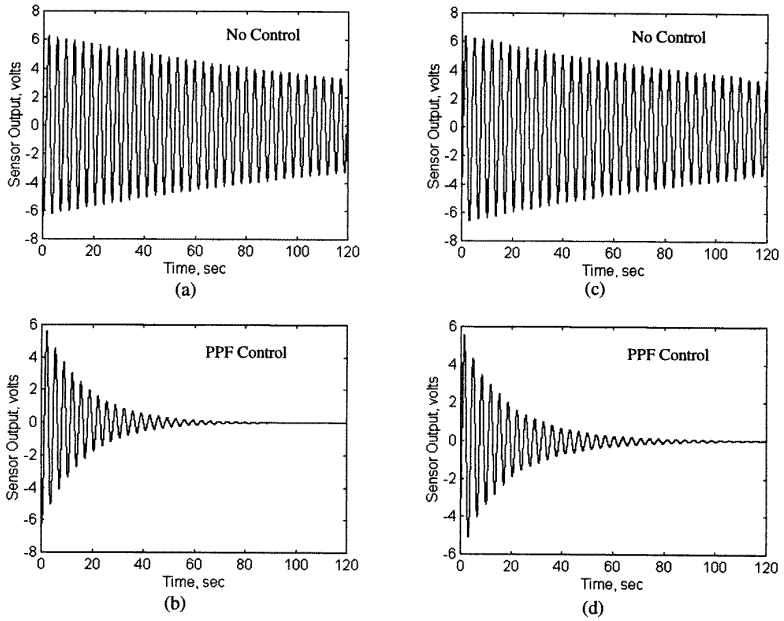

Figure 10. Simulation (left) and experimental (right) results of implementing a PPF controller on a first-mode excitation.

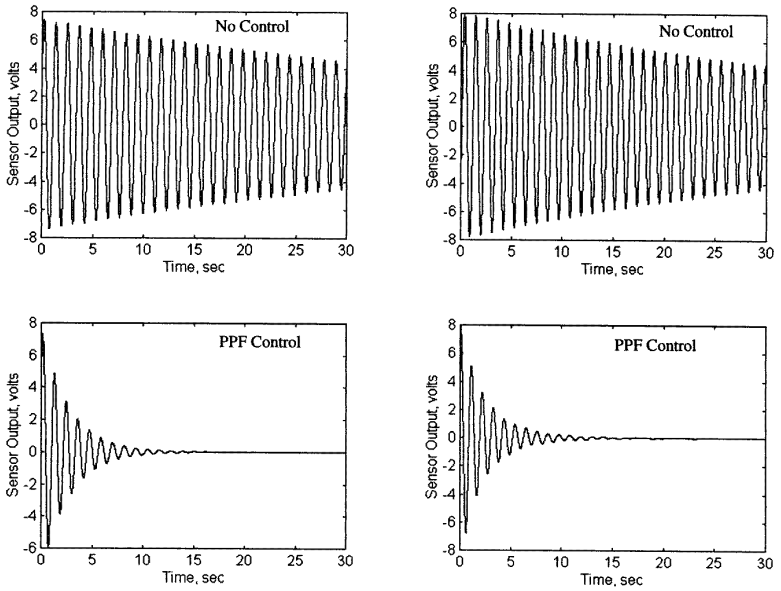

Figure 11. Simulation (left) and experimental results (right) of implementing a PPF controller on a second-mode excitation.

with a performance enhancement for the second mode. Figure 12(d) is similar to figure 12(c) with the exception of an increased gain on the base arm actuator to enhance first-mode damping characteristics.

5.3. LQG experiments

The performance of the LQG controller was evaluated in terms of the displacement of the tip of the beam, measured by a CCD camera. This controller used two actuators, as discussed previously. The states which were not measured were estimated using a Kalman filter.

The values of Q, the output weighting matrix, and R, the control weighting matrix, were determined from simulations as

$$Q = \begin{bmatrix} 100 & 0 & 0 & 0 & 0 & 0 \\ 0 & 100 & 0 & 0 & 0 & 0 \\ 0 & 0 & 1 & 0 & 0 & 0 \\ 0 & 0 & 0 & 1 & 0 & 0 \\ 0 & 0 & 0 & 0 & 9000 & 0 \\ 0 & 0 & 0 & 0 & 0 & 900\,000 \end{bmatrix}$$

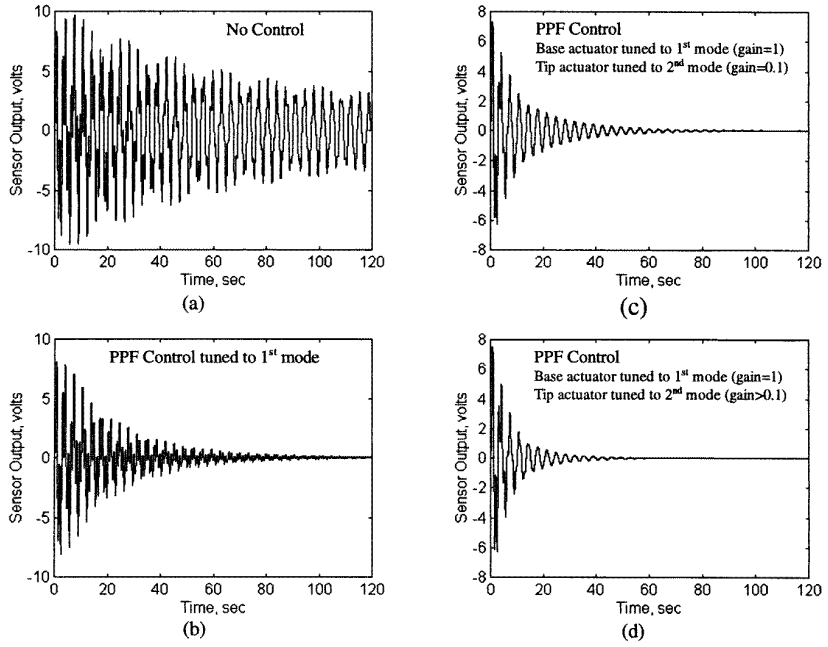

Figure 12. Experimental results of implementing a PPF controller on a multiple-mode excitation.

$$R = \begin{bmatrix} 0.1 & 0 \\ 0 & 0.1 \end{bmatrix}$$

where the sensor output vector, y, contains the piezoceramic sensors as the first two elements (volts) and four VisionServer outputs (elbow displacement, elbow rotation, tip displacement and tip rotation) as the last four elements (meters and radians, respectively) of the output vector. The two control inputs (volts) are the base actuator and the elbow actuator, respectively. These values kept the control inputs within their limitations of ± 150 volts, the sensors within their limitations of ± 10 volts, minimized the steady state error and met a 20 second settling time constraint.

For the Kalman filter design, the plant uncertainty matrix, F, is the identity matrix and the model uncertainty (W) is approximated at 5%. The sensor process noise as taken as the squares of component rms noise values (V matrix diagonal elements) from documentation and previous research.

$$W = 0.05[I]$$

$$V = \begin{bmatrix} 0.0001 & 0 & 0 & 0 & 0 & 0 \\ 0 & 0.0001 & 0 & 0 & 0 & 0 \\ 0 & 0 & 0.000\,25 & 0 & 0 & 0 \\ 0 & 0 & 0 & 0.002 & 0 & 0 \\ 0 & 0 & 0 & 0 & 0.000\,25 & 0 \\ 0 & 0 & 0 & 0 & 0 & 0.001 \end{bmatrix}.$$

Figure 13 shows the performance of the controller for a first-mode response. Figure 14 shows the performance for a multi-mode excitation (first and second modes). From table 5 it is clear that LQG control is very effective in the case of multi-mode excitation.

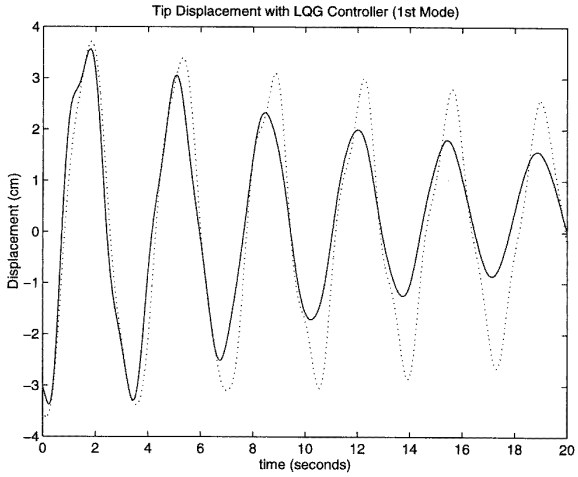

Figure 13. Experimental results of tip displacement of the LQG controller on a single-mode excitation (dashed line—no control; solid line—LQG control).

Table 5. Comparison of damping ratio.

	No control	LQG	Increase (%)
1st mode	0.004	0.0367	817.5
2nd mode	0.004	0.0678	1595

6. Conclusions

This paper discusses techniques of active vibration suppression utilizing piezoelectric actuators. The investigations, including both simulations and experiments, were conducted on the Naval Postgraduate School's flexible spacecraft sim-

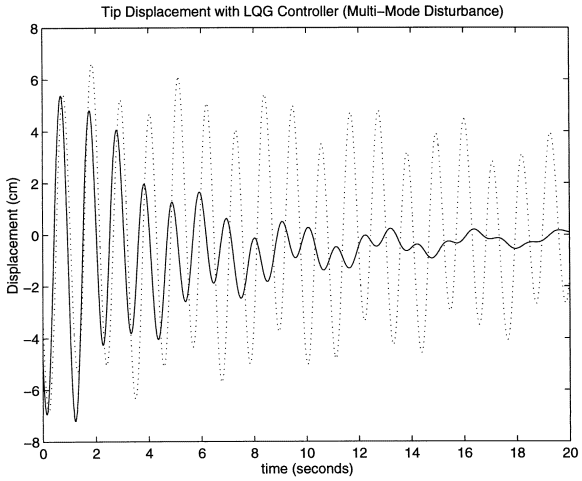

Figure 14. Experimental results of tip displacement of the LQG controller on a multi-mode excitation (dashed line—no control; solid line—LQG control).

ulator (FSS). The FSS simulates motion about the pitch axis of a spacecraft and is comprised of a rigid central body and a flexible appendage. A positive position feedback (PPF) controller was designed to actively damp vibration induced in the flexible appendage. The PPF controller was implemented using piezoceramic actuators and sensors. Both single-mode and multiple-mode oscillations were induced in the flexible appendage. For a single-mode excitation, damping in the appendage increased significantly with the PPF controller tuned to this particular frequency. For multiple-mode excitation, PPF produced limited damping enhancement. Experimental results closely paralleled numerical simulations. Furthermore, a linear–quadratic Gaussian (LQG) controller was applied to minimize the tip movement. The LQG controller was implemented using piezoceramic actuators and sensors, and the tip displacement and rotation were sensed by LEDs and an optical infrared camera. LQG was proved experimentally an effective method to damp out multi-mode excitation of the flexible appendage but not as effective as the PPF controller for single-mode vibration suppression.

References

Agrawal B N 1996 Spacecraft vibration suppression using smart structures *4th Int. Congress on Sound and Vibration (St Petersburg, 1996)* pp 563–70

Agrawal B N and Bang H 1994 Adaptive structure for large precision antennas *45th Congress Int. Astronaut. Federation (Jerusalem, 1994)*

Fanson J L and Caughey T K 1990 Positive position feedback control for large space structure *AIAA J.* **28** 717–24

Feuerstein M G 1994 A comparison of different control methods for vibration suppression of flexible structures using piezoelectric actuators *Master Thesis* US Naval Postgraduate School

Gobinathan M and Pajunen G A 1995 Model reference control of vibrations in flexible smart structures *Proc. IEEE 34th Conf. Decision and Control* pp 3551–6

Goh C J and Caughey T K 1985 On the stability problem caused by finite actuator dynamics in the collocated control of large space structure *Int. J. Control* **41** 787–802

Newman S M 1992 Active damping control of a flexible space structure using piezoelectric sensors and actuators *Master Thesis* US Naval Postgraduate School

Smith R S, Chu C C and Fanson J L 1994 The design of H_∞ controllers for an experimental non-collocated flexible structure problem *IEEE Trans. Control Syst. Technol.* **CST-2** 101–9

Won C C, Sulla J L, Sparks D W Jr and Belvin W K 1994 Application of piezoelectric devices to vibration suppression *J. Guidance Control Dynam.* **17** 1333–8

Zeinoun I and Khorrami F 1994 *Fuzzy Based Adaptive Control for Flexible-link Manipulators Actuated by Piezoceramics* pp 643–8